Ultrasound imaging velocimetry in a dense two-phase swirling flow

Holemans, Thomas; Hogendoorn, Willian; Poelma, Christian; De Greef, Johan; Vanierschot, Maarten

DOI
10.1007/s00348-024-03896-9

Publication date
2024

Document Version
Final published version

Published in
Experiments in Fluids

Citation (APA)
Holemans, T., Hogendoorn, W., Poelma, C., De Greef, J., & Vanierschot, M. (2024). Ultrasound imaging velocimetry in a dense two-phase swirling flow. *Experiments in Fluids*, *65*(11), Article 158. https://doi.org/10.1007/s00348-024-03896-9

Experiments in Fluids (2024) 65:158
https://doi.org/10.1007/s00348-024-03896-9

RESEARCH ARTICLE

Ultrasound imaging velocimetry in a dense two-phase swirling flow

Thomas Holemans[1] · Willian Hogendoorn[2] · Christian Poelma[3] · Johan De Greef[4] · Maarten Vanierschot[1,5]

Received: 7 July 2024 / Revised: 23 September 2024 / Accepted: 28 September 2024

Abstract

Ultrasound imaging velocimetry (UIV) is a maturing technique for measuring the dispersed phase in two-phase flows. It enables measurements of dense suspensions when optical methods fail. This study explores UIV's applicability to measure the flow field in a swirling flow reactor (SFR) for solid–liquid mixing of dense suspensions. Despite UIV's historical focus on unidirectional flows like arteries and axisymmetric pipes, this research demonstrates its adaptation to an inherently complex 3D flow field, i.e., a swirling sudden expansion flow in an SFR. Using high-speed plane-wave imaging and correlation averaging techniques, satisfactory velocity profiles are achieved while preserving sufficient temporal information. Firstly, the applicability of UIV in this specific setup is demonstrated by comparing UIV with stereoscopic particle image velocimetry measurements of a single-phase flow in the SFR, both indicating a Coandă jet flow (CoJF). Secondly, several bulk velocities and volume concentrations (up to 50 vol%) are measured with UIV for a suspension of water and 2.3-mm glass beads. A transducer is installed in two orientations and captures all three velocity components when combining the two datasets. A timestep optimization process is implemented to avoid the need for manual finetuning of the acquisition frequency. A time-domain spectral analysis on the dispersed phase velocity fields in the SFR reveals dominant frequencies between 1.21 and 2.42 Hz, similar to those found in single-phase flow. The general flow structure of the dispersed phase in suspension is very similar to the latter; however, the addition of particles confines the central recirculation zone (CRZ) to the center. Finally, the implementation of swirl to keep solid–liquid mixtures in suspension in the SFR is experimentally confirmed by this study. Quantitative UIV measurements confirm favorable flow structures for mixing, specifically a CoJF that avoids sedimentation. The concentration of solids in an SFR can even be increased up to 50 vol% while still maintaining a uniform suspension.

1 Introduction

Efficient solid–liquid mixing is pivotal in various chemical processes, encompassing catalytic reactions, hydrogenation, crystallization, leaching, precipitation, and many more (Carletti et al. 2014; Shi and Rzehak 2020). Stirred tank reactors (STRs) have dominated these applications, representing over 95% of industrial use cases. This dominance stems from their relative simplicity and continuous enhancement of energy and economic efficiency over the years (Barabash et al. 2018; Jaszczur and Młynarczykowska 2020). However, their reliance on rotating components within the working

---

✉ Maarten Vanierschot
maarten.vanierschot@kuleuven.be

Thomas Holemans
thomas.holemans@kuleuven.be

Willian Hogendoorn
w.j.hogendoorn@tudelft.nl

Christian Poelma
c.poelma@tudelft.nl

Johan De Greef
johan.degreef@kuleuven.be

[1] Department of Mechanical Engineering, Group T Leuven Campus, KU Leuven, Andreas Vesaliusstraat 13, 3000 Leuven, Belgium

[2] Complex Fluid Processing (ME-P&E), Delft University of Technology, Leeghwaterstraat 39, 2628 CB Delft, The Netherlands

[3] Multiphase Systems (ME-P&E), Delft University of Technology, Leeghwaterstraat 39, 2628 CB Delft, The Netherlands

[4] Department of Materials Engineering, Group T Leuven campus, KU Leuven, Andreas Vesaliusstraat 13, 3000 Leuven, Belgium

[5] Material Science, Innovation and Modelling (MaSIM), North-West University, Private Bag X2046, Mmabatho 2745, South Africa

volume introduces challenges such as leaks, wear, and friction under extreme conditions, particularly as systems scale up or handle higher volume concentrations (Pangarkar 2017; Jaszczur and Młynarczykowska 2020). Moreover, promising new technologies are limited in industrial production by the lack of high-temperature, high-pressure solid–liquid mixing technologies at an industrial scale.

To address the limitations discussed above and create new ways for industrial-scale solid–liquid mixing at high temperatures and pressures, swirling flow reactors (SFRs) are proposed as novel technology (Yang et al. 2023; Yang 2023). An SFR is conceived as a swirling sudden expansion of solid–liquid flow, possibly with a filter at the outlet to entrap solid particles in the reactor. Computational fluid dynamics (CFD) simulations already demonstrated the SFR's working principle (Yang et al. 2023; Yang 2023). Yang et al. (2023) performed an Eulerian–Eulerian simulations of an SFR, in conjunction with an RNG k–ϵ turbulence model, at 20 vol% wood spheres. In a follow-up research (Yang 2023), they have shown that an SFR works for higher volumetric loadings by performing simulations at 40 vol%. Extensive simulations for parametric analysis or design purposes must rely on turbulence models (e.g., aforementioned k–ϵ) instead of fully resolved direct numerical simulation (DNS). The latter are computationally too expensive, especially for particle-laden flows (Brändle De Motta et al. 2019). The considered fluid was supercritical methanol at 235 °C and 130 bar, resulting in a density ratio of 1.7.

Experimental data are essential to increase the validity of CFD simulations (Oberkampf and Trucano 2002). This is, in particular, the case for swirling flows, as a small variation or disturbance in the inlet flow will affect the flow regime or patterns in the reactor. The latter includes phenomena such as vortex breakdown, vortex core precession and large-scale coherent structures (Kuzmin 2021). Therefore, experimental data in conjunction to CFD simulations are required to validate whether the correct flow regime is studied. Established methods that measure quantitative flow fields and validate CFD results typically include optical techniques like particle image velocimetry (PIV) or laser Doppler velocimetry (LDV). Whereas they are recognized as superior in single-phase flows, these techniques are of limited value in turbid flows. Optical measurements are limited for dispersed phase fractions as low as 0.5 vol%, without changing the system (Montante et al. 2012; Deen et al. 2002; Poelma et al. 2006). This limit can be extended by refractive index

Fig. 1 Schematic drawing and photograph of the SFR

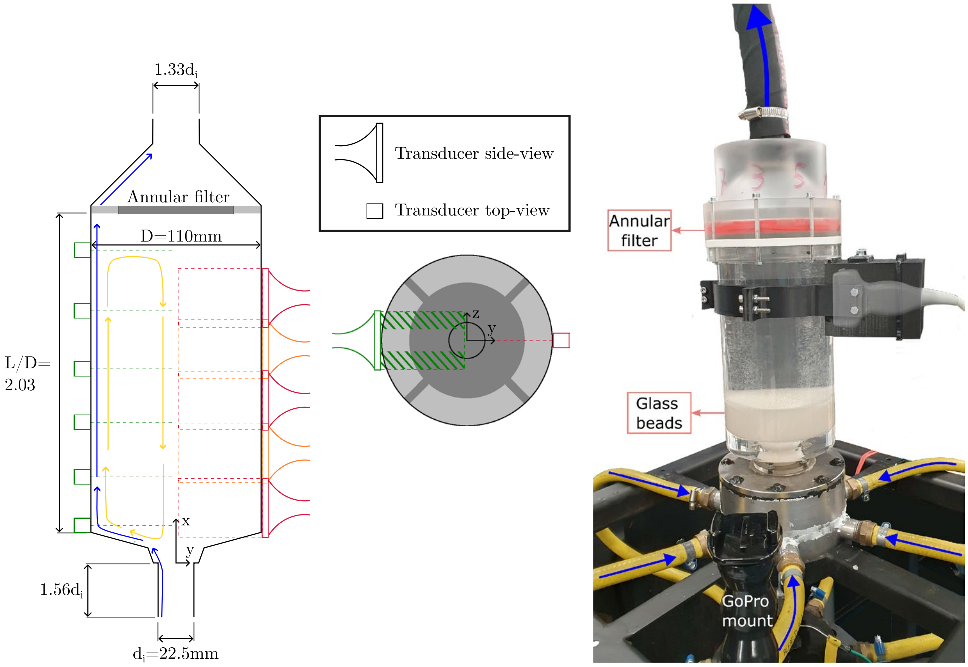

(a) Schematic drawing of the SFR with the inlet at the bottom and the outlet at the top. Left: side view, right: top view. The horizontal measurements ($y-z$ plane) are shown in green, while the vertical measurements ($x-y$ plane) are shown in alternating orange or red. A legend of transducer orientation is added at the top right. On the reactor's left side, the envisioned flow patterns are depicted in blue and yellow, for the fluid and dispersed phase, respectively.

(b) Photograph of the measurement section and the UIV-transducer installed in its respective mount for a vertical measurement. A photograph of the transducer is imposed on the mount to show its internal position. The flow direction in the tubes is indicated with blue arrows. At the bottom of the reactor, sedimented glass beads are visible.

matching (RIM) liquid and solids, but the system's complexity is thereby increased. A *'dense'* solid–liquid suspension in the literature is considered to have a solids volume fraction of around 8 vol%, which is in general regarded as the limit of optical techniques with RIM (Li et al. 2018; Zachos et al. 1996; Wright et al. 2017; Poelma 2020). Wiederseiner et al. (2011) have shown that for some specific liquid–solid combinations with near-perfect temperature control, higher volume fractions are feasible. However, the strict requirements on both the fluid and the solids severely increase the complexity of experimental setups and limit the physical conditions that can be measured. A mismatch of 0.2% in the refractive indices renders the images unusable (Dijksman et al. 2012; Poelma 2020). The current study considers volumetric loadings of 20 vol% and higher, making optical measurement techniques unfeasible (Wiederseiner et al. 2011; Wright et al. 2017).

UIV or echo-PIV, a technology that has matured in the last decade, emerges as a promising alternative for characterizing flows not accessible to optical measurement techniques (Poelma 2017, 2020). It acquires images using an ultrasound transducer and yields velocity fields from these images with similar processing algorithms to PIV. The most common field of application is the medical field, where optical access to arteries is not feasible, and ultrasound imaging devices are commonly used instead (Hoving et al. 2021; Brum et al. 2021). The signal-to-noise ratio (SNR) and resolution are relatively low for UIV compared to PIV, and the resolution differs between the parallel and perpendicular direction to the transducer (Poelma 2020). Tracer materials designed for ultrasound imaging, like ultrasound contrast agents, improve the SNR. The main downside of these contrast agents is the cost and the relatively short lifetime in larger experimental setups (Fraser et al. 2017; Zhang et al. 2011; Poelma 2020). The reflected ultrasound signal is attenuated as it travels deeper into the measurement volume. This can be compensated with a time gain compensation to obtain equal intensity throughout the whole measurement area. The SNR, however, still decreases deeper into the system since the noise, due to the increasing number of interfaces, is also amplified.

Another approach for increasing the SNR is correlation averaging over several frames to improve the data quality in transient flows (Dash et al. 2022; Poelma et al. 2011). This averaging is only possible if the transient phenomena are significantly slower than the acquisition frequency, since some temporal information is lost. UIV conventionally collects data by sequentially reading out a phased-array transducer, implying that a UIV image is constructed of signals obtained at different times (Poelma 2017). An alternative approach is plane-wave imaging, where all transducer elements are used simultaneously (Tanter and Fink 2014). Plane-wave imaging decreases the SNR further, but the increase in image rate enables correlation averaging while maintaining sufficient temporal resolution (Hogendoorn and Poelma 2019; Dash et al. 2022). UIV has been successfully applied for characterizing suspension pipe flows under both laminar (Hogendoorn et al. 2023, 2021; Hogendoorn and Poelma 2018; Dash et al. 2021; Walker et al. 2014) and turbulent conditions (Hogendoorn et al. 2021; Dash et al. 2021; Gurung and Poelma 2016; Barnes et al. 2024).

This research aims to extend UIV to a highly three-dimensional flow, specifically a swirling sudden expansion two-phase flow, based on the SFR design by Yang et al. (2023). In the next section, the experimental setup and data processing will be discussed. Following, single-phase flow measurements using UIV and stereoscopic particle image velocimetry (S-PIV) are compared. After validation of the measurement technique in a single-phase flow, dispersed solid phase flow measurements in a dense suspension are performed. Finally, the main conclusions of all measurements are discussed.

2 Experimental setup and data processing

2.1 Experimental setup

Experiments are performed in an SFR, consisting of a sudden expansion with a step and two tapered parts, similar to the design of Yang et al. (2023). The dimensions with the envisioned flow patterns visualized for both the liquid and dispersed phase are shown in Fig. 1a. The first tapered part has a radial dimension $0.16\,d_\mathrm{i}$ and is installed at 20°, while the second tapered part has a radial dimension of $1.63\,d_\mathrm{i}$ and is installed at 75°. Both angles are measured from the centerline (x-axis). A photograph of the SFR with sedimented glass beads is shown in Fig. 1b. UIV measurements are taken either in vertical $x-y$ planes or in horizontal $y-z$ planes. A variable swirling flow can be fed into this setup by a swirl generator from the IFRF burner series, more specifically, the 30 kW series (Dugué and Weber (1992)). This swirl generator is used in numerous studies as an annular swirling jet (Zhang and Vanierschot 2021; Vanierschot et al. 2020; Vanierschot 2007) and as a round (free) jet (Holemans et al. 2023a, b; Vanierschot 2018; Holemans et al. 2024). For this study, the annular tube is removed and a confinement is added, converting it to a round jet. A detailed view of the cross section of the swirl generator can be seen in Fig. 2a. The guide vanes are rotated to generate the maximum swirl number achievable for which their position is depicted in Fig. 2b.

The swirl number considered is $S_{0.84}$, which is the conventional swirl number adjusted to only include 84% of the total inlet pipe's diameter (d_i):

Fig. 2 Schematic representation of the swirl generator and positioning of the guide vanes

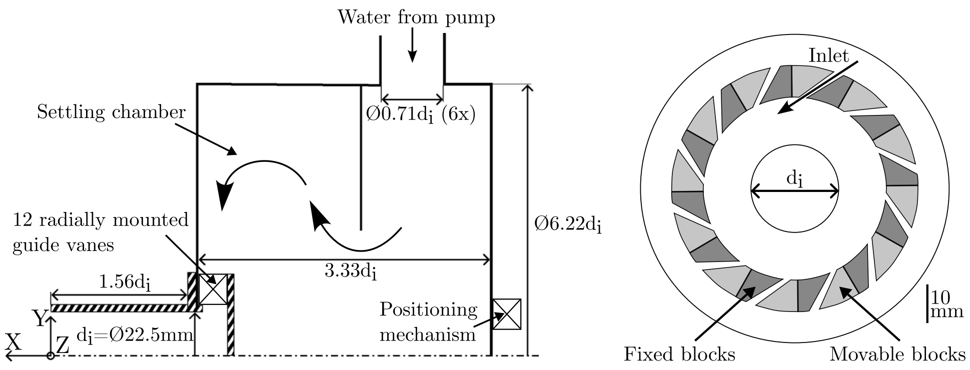

(a) 30 kW movable block swirl generator as designed by Dugué and Weber [36].

(b) Position of the guide vanes of the swirl generator to produce a maximal swirling inlet flow.

$$S_{0.84} = \frac{\int_0^{0.42\,d_\mathrm{i}} \overline{u}\,\overline{w}\,r^2\,\mathrm{d}r}{\frac{d_\mathrm{i}}{2}\int_0^{0.42\,d_\mathrm{i}} \overline{u}^2\,r\,\mathrm{d}r}, \tag{1}$$

where r is the radial position in the inlet tube, with an absolute maximum of $d_\mathrm{i}/2$ and a maximum of $0.42\,d_\mathrm{i}$ in the previous formula. The swirl number is experimentally calibrated with LDV, resulting in a value of $S_{0.84} = 1.87 \pm 0.09$, as elaborated in previous work (Holemans et al. 2024). Upstream of the movable block swirl generator, the flow is divided into six separate channels to feed the settling chamber, seen as the yellow tubes in Fig. 1b. The flow is provided by a frequency-controlled centrifugal pump (Packo NP/68-50/152), with a nearly flat pump curve for the volumetric flows considered in this study. The maximum frequency of the pump is set to 50 Hz. The flow rate is measured by a Gardena™ flow meter (type 8188-20), having a 2% measurement error after calibration. The calibration is done by weighing mass outflow at the studied flowrates. During dispersed phase flow measurements, the flow rate is manually adjusted, to achieve the most visually homogeneous suspension possible. The outlet contracts at 45°, to an outlet diameter of $4/3\,d_\mathrm{i}$. An annular outlet with a blockage ratio of 45% is installed at $x/d_\mathrm{i} = 10.2$, indicated in Fig. 1b. Between the annular hub and the outer rim a filter mesh is installed, entrapping particles in the reactor. The four ribs connecting the filter's annular hub to the outer rim block an extra 4% of the total area, depicted as dark gray in Fig. 1a. The cylindrical reactor vessel is made of transparent polymethyl methacrylate (PMMA). The UIV transducer is placed against the outer reactor wall using a dedicated 3D printed mount that allows for reproducible positioning, seen in black in Fig. 1b. Aquasonic® gel is applied between the transducer and the cylinder to ensure the propagation of sound waves in the reactor. Glass spheres, designed for water filtration, with a diameter of 2.27 ± 0.01 mm are used as solid particles in the reactor. The particles have an aspect ratio of 0.96 ± 0.004 and a density of 2570 kg/m^3. For each measurement, the temperature and average flow rate are measured. The flow is characterized by the suspension Reynolds number:

$$\mathrm{Re}_\mathrm{s} = \frac{\overline{u}_\mathrm{inlet}\,d_\mathrm{i}\,\rho_\mathrm{f}}{\mu_\mathrm{s}}, \tag{2}$$

where $\overline{u}_\mathrm{inlet}$ is the mean bulk inlet velocity, ρ_f the fluid density, and μ_s the effective viscosity of the suspension. The latter is obtained from Eilers' viscosity model (Stickel and Powell 2005; Ferrini et al. 1979; Eilers 1941). The spheres are considered perfect spheres with a maximum packing density of 0.64 (Desmond and Weeks 2014). Re_s varies between 1,600 and 23,900 for the different volume fractions. For reference, the Reynolds number based on the single-phase viscosity varies between 23,300 and 44,400 for the suspension measurements.

2.2 Data acquisition

The data in this study are obtained using a Verasonics Vantage 128™ research ultrasound system with a linear transducer (L11-5v). Additionally, an S-PIV-measurement for single-phase flow is performed in the same setup at a slightly higher Reynolds number ($Re = 21,300$). The specific settings of the ultrasound system for both the single-phase and suspension measurements are discussed in the following paragraph. If these settings differ, the single-phase settings precede the suspension settings in the text.

To enhance either the radial resolution or penetration depth, respectively, the transducer operates at a frequency of 10.5 MHz or 7.5 MHz. Additionally, bandwidths of 9.0–12.0 MHz or 6.5–8.5 MHz are prescribed, resulting in a satisfactory image quality after visual inspection. The transducer consists of 128 individual elements with a pitch of 0.3 mm each, resulting in a field of view of 38.4 mm, along the transducer. The field of view's depth within the

Fig. 3 Schematic representation of acquisition and processing structure for multi-pulse datasets, depicting subset-correlation-averaging and full-correlation-averaging

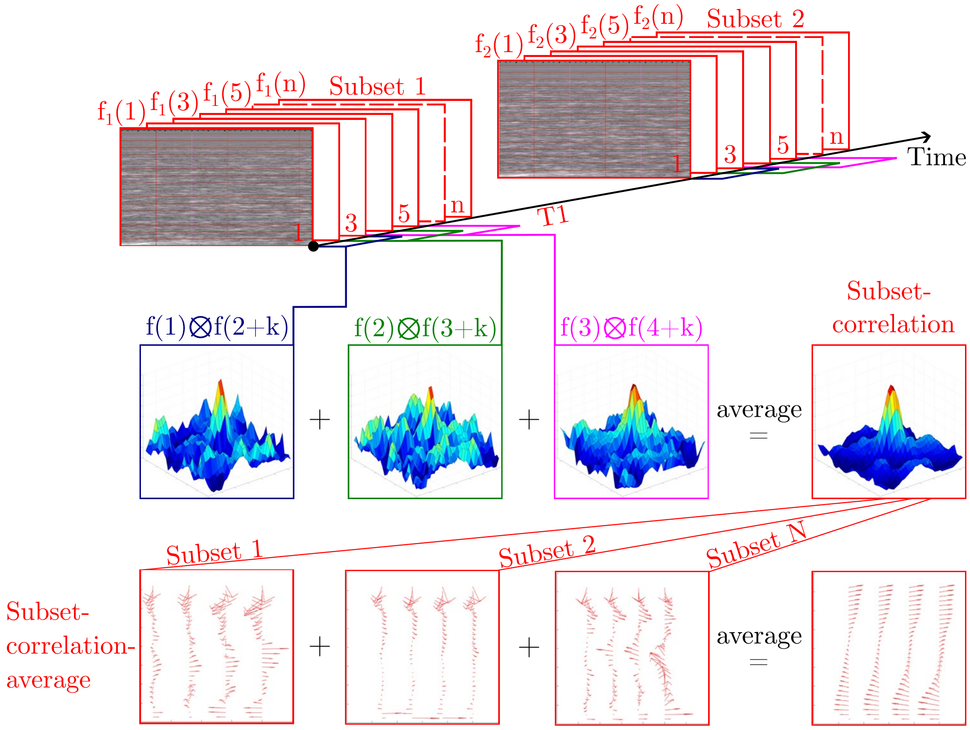

(a) Acquisition structure and processing structure depicting subset-correlation-averaging.

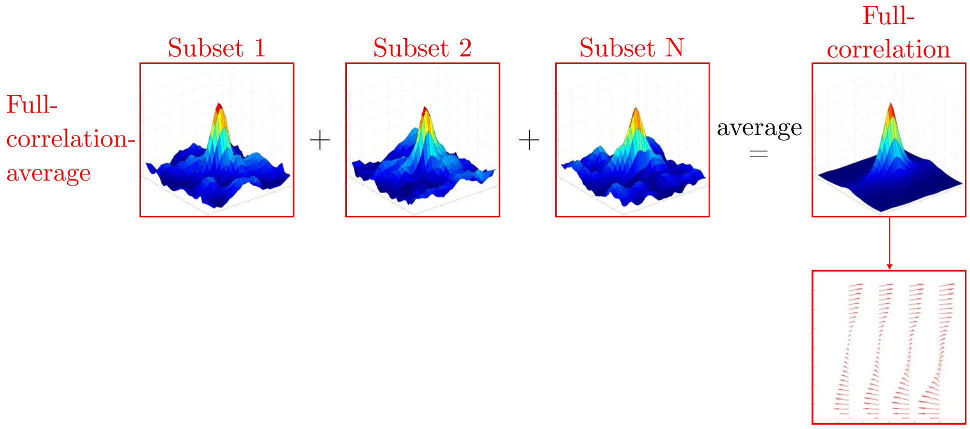

(b) Acquisition structure and processing structure depicting full-correlation-averaging. The correlation peaks are referring to the subset-correlations of Figure 3a.

reactor, already accounting for the 5-mm PMMA wall, is established at 53.6 mm or 52.9 mm, close to the reactor's center at 55 mm. For the vertical measurements, the radial velocities (y-axis) have a higher resolution than the axial velocities (x-axis). For the horizontal measurements the tangential velocities (z-axis) have the lowest resolution. The transducer has an elevational focal depth of 18 mm.

The image acquisition frequency is 1200 Hz or between 2000 and 10,000 Hz. The suspension measurement's acquisition frequency is lowered if the particles visually move slowly in the measurement volume, which is only the case for high volumetric loadings. These signals are converted to brightness-mode (B-mode) images, and only these are stored to reduce data usage. To allow correlation averaging, consecutive image series (subsets) are acquired, depicted in Fig. 3 as 'Subset 1' and 'Subset 2'. Acquiring data in different temporally spaced subsets increases the number of uncorrelated samples. The total number of subsets is determined by the RAM capacity of the imaging system. An amount of N subsets are acquired, totaling 4,800 or 8,100 images, either in sets of 10 or 30 images, with a time delay (T_1) of 100 or 167 ms.

The downside of acquiring temporally spaced subsets is that high-frequency signals will not be distinguishable in a time-domain spectral analysis. A time-resolved dataset is added to check for high-frequency structures for two

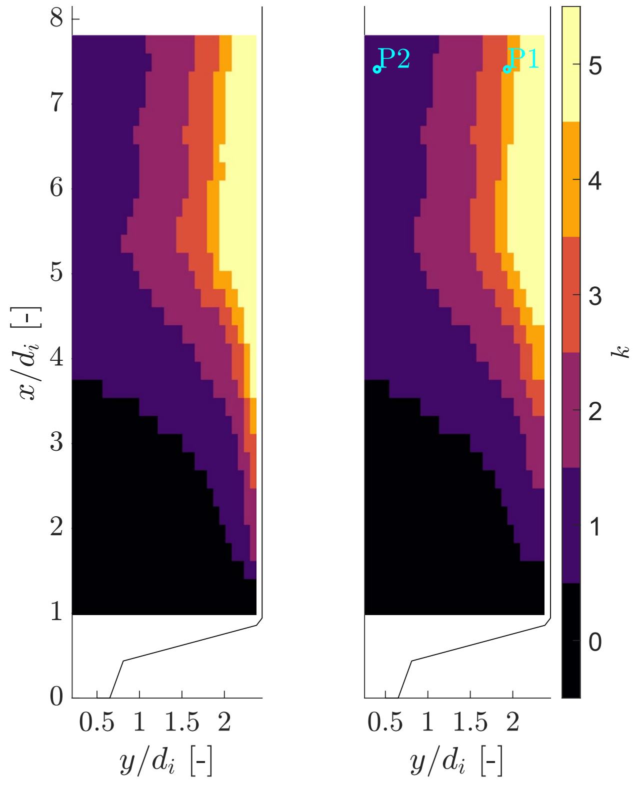

(a) Original data

(b) Smoothed data

Fig. 4 Optimal value of k, based on $C(k)$ throughout the domain, both original and smoothed. The values of $C(k)$ are plotted for several values of k in Fig. 5

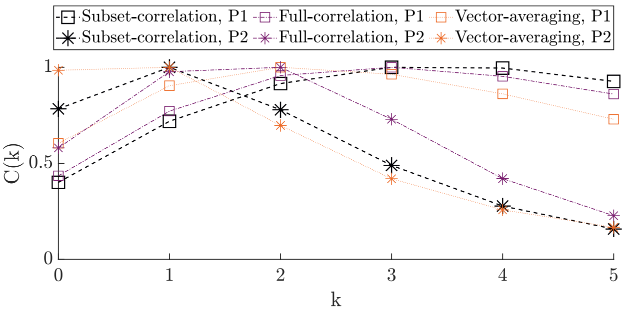

Fig. 5 $C(k)$ for each processing algorithm plotted for the two positions indicated as *P1* & *P2* in Fig. 4

volumetric loadings considered in this study. Horizontal datasets are included for the suspension measurements (depicted in green in Fig. 1a). Lastly, the increased number of images per subset for the suspension datasets allows for finetuning the value of k for each dataset, where k indicates the number of frames skipped for a cross-correlation. The next section provides a more detailed explanation.

For single-phase measurements, Vestosint® particles are used as tracer particles, with a mean diameter of 56 µm and a density of 1.016 g/cm^3. The Reynolds number for these measurements is 17,900 , resulting in a particle relaxation time of 0.18 ms. The Stokes number is 0.006, indicating acceptable flow tracing accuracy (Raffel et al. 2018). The characteristic time scale is defined as the ratio between the nozzle diameter and $\overline{u}_{\text{inlet}}$. Furthermore, these particles exhibit favorable acoustic properties and have been utilized in previous studies for both optical PIV measurements (Scarano and Poelma 2009) and UIV measurements (Hogendoorn and Poelma 2019; Gurung and Poelma 2016).

2.3 Data processing

The correlations from each subset are summed to increase the SNR while maintaining temporal low-frequency dynamics. This is visually illustrated above the double black line in Fig. 3. A vector field for each subset is obtained, and this method is labeled subset-correlation-averaging. Summing each subset's correlation values together to acquire only one final vector field is referred to as full-correlation-averaging, visualized below the double black line in Fig. 3. This method is identical to the average correlation method of Meinhart et al. (2000) which is also coined sum-of-correlation in some sources. Within one subset both subset- and full-correlation-averaging are identical, performing a sum-of-correlation. However, across subsets the methods differ which motivates the introduction of the two new terms. A third possibility for processing the datasets, called vector-averaging, is not adding correlations and using each pair of images to get a vector field. Lastly, a time-resolved dataset can be acquired where sliding sum-of-correlation is used to increase the SNR to only lose limited temporal information. A multi-pass PIV processing algorithm with an initial interrogation window of 48x48 and a final interrogation window of 32x32 pixels, with 50% overlap, is used for processing all the datasets. Since the data are acquired with a MATLAB script and saved in MATLAB variables, PIVlab (Thielicke and Stamhuis 2014) is used as PIV processing software to acquire the vector fields from the B-mode images. The code is slightly adjusted to allow correlation averaging of each separate subset and outputting its vector field. For the S-PIV measurements, a multi-pass algorithm in Davis 10.1.2 is utilized, with self-calibration and 50% overlap. Possible erroneous vectors are removed with a low correlation rejection and a 4-pass regional median filter, more information on the S-PIV setup can be found in a previous publication (Holemans et al. 2024). Based on the S-PIV flow fields, the UIV acquisition frequency is manually finetuned to yield satisfactory results. The vector spacing in S-PIV is 0.77×0.77 mm^2 compared to UIV with 4.8×1.12 and 4.8×1.55 mm^2, for single-phase and suspension flow measurements, respectively. The vertical UIV data are acquired with an overlap between different datasets, this enables stitching of these datasets in post-processing. The datasets are linearly interpolated into a structured grid to get vectors at regular intervals while maintaining their original resolution. The S-PIV dataset, only containing data for $0.93 \leq x/d_\mathrm{i} \leq 5.42$, is linearly interpolated to an identical grid.

The dispersed phase's flow structures and velocities are unknown beforehand in the suspension; the following cost function, $C(k)$, is introduced to avoid manual iterative optimization of the acquisition frequency for each dataset:

$$C(k) = c_k^2 \sqrt{u_{p,k}^2 + \left(v_{p,k}\frac{\mathrm{d}y}{\mathrm{d}x}\right)^2}\, n_{\mathrm{interpolated},k}, \tag{3}$$

where c_k is the cross-correlation value between an image pair or a sum of cross-correlation values. $u_{p,k}$ is the velocity along the transducer, and $v_{p,k}$ is the velocity perpendicular to the transducer. $\frac{\mathrm{d}y}{\mathrm{d}x}$ is added to correct for the difference in resolution, where $\mathbf{d}y$ and $\mathbf{d}x$ are the resolution along and perpendicular to the transducer, respectively. $n_{\mathrm{interpolated},k}$ is zero if a specific vector is deleted during the post-processing step, and it has a value of unity if the vector is retained. In the first processing round ($k = 0$), each frame is cross-correlated with its subsequent frame ($f(1) \bigotimes f(2+k)$). In the next round, the skip factor (k) is increased to 1, and each frame is cross-correlated with its second subsequent frame, as indicated in Fig. 3. This process is repeated up until $k = 5$. $C(k)$ is calculated for each vector position, and its maximum value is taken as the ideal value of k for this respective vector. This cost function allows us to perform the bulk of the measurements at identical acquisition frequency and finetune the time interval in post-processing. A similar procedure of locally optimizing the time interval is explained for time-resolved PIV by Hain and Kähler (2007); however, they use the velocity field of the first cross-correlation ($f(1) \bigotimes f(2)$)

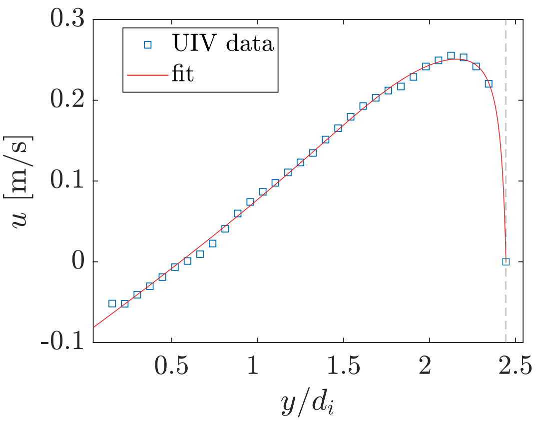

Fig. 6 Single vector row for a typical suspension flow case at $x/d_\mathrm{i} = 1.4$. The continuous curve is a fit to the UIV data and considered to be the average velocity field. A vertical dashed line is added to indicate the location of the reactor wall

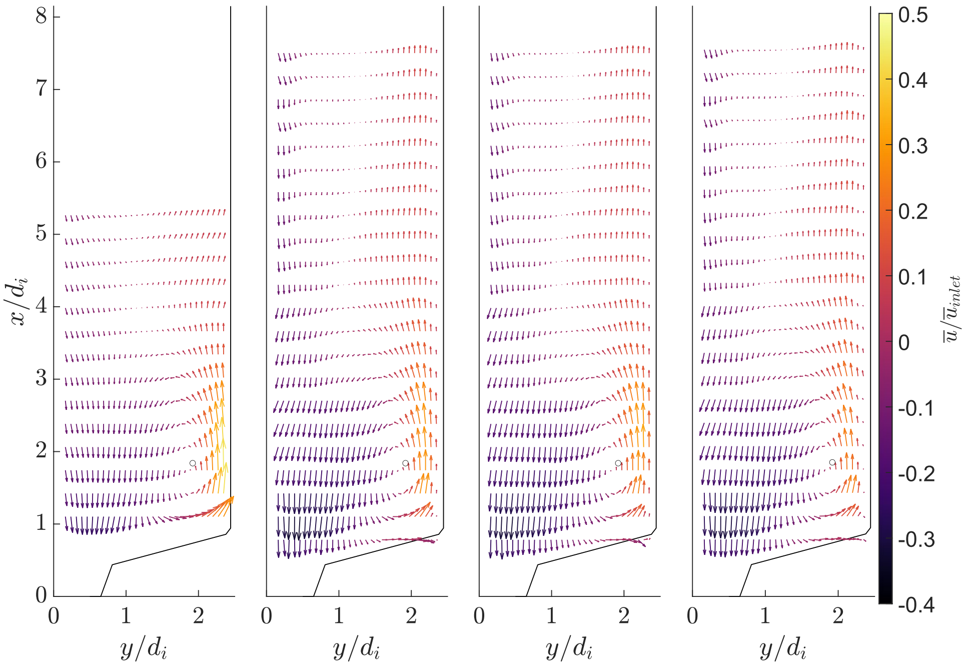

(a) Reference S-PIV measurements

(b) UIV, subset-correlation-averaging

(c) UIV, full-correlation-averaging

(d) UIV, vector-averaging

Fig. 7 Average in-plane velocity vectors for the measured regions of the S-PIV and UIV measurements, colored by their axial velocity. The reactor's outline is depicted as a solid black line. For the UIV measurements, different results for each processing method are depicted and the vector spacing is increased with 50% for readability as an initial guess for the ideal local value of k, after which they perform a validation.

To avoid any local outliers for k, a median filter of 3×9 vectors along and perpendicular to the transducer, respectively, is applied to smoothen the field. The optimal value of k is depicted in Fig. 4 for a reference dataset at 50 vol%, also showing the effect of the median filter. Deeper into the reactor, lower values of k are obtained due to the decreasing correlation value for the increasing distance from the transducer. Additionally, the influence of the slower downstream flow is visible as the optimal value of k increases downstream.

Due to the iterative procedure and possible higher values of k, more frames for each subset are required, which is why thirty frames are acquired instead of ten as is the case for the single-phase measurements. The local value of $C(k)$ is indicated for two specific vectors in Fig. 5. The values of $C(k)$ are normalized. For vector *P1*, the highest value is achieved at $k = 3$ for both full- and subset-correlation-averaging, with slightly higher values for full-correlation-averaging at higher values of k due to its increased SNR, and subsequent limited amount of vector rejections. The vector-averaging's peak value is at $k = 2$, with a similar value at $k = 1$; this indicates that the vector-averaging's SNR is lower, as expected. Higher values of k increase both turbulence decorrelation and loss of particles in the particle images due to out-of-plane motion. For measurements further from the wall, i.e., vector *P2*, full-correlation-averaging reaches a peak value at $k = 2$, with a nearly identical value at $k = 1$. For subset-correlation-averaging, there is a clear peak at $k = 1$. The vector-averaging's peak is at $k = 1$, with a nearly identical value at $k = 0$. It is clear from these data that for measurements further away from the wall, at least some form of correlation averaging, like subset-correlation-averaging, is needed to increase the SNR to acceptable values. The ideal value of k is proportional to the flow speed and inversely proportional to the measurement depth.

The post-processing of the vector fields consists of three different steps. First, a velocity limit is applied where the absolute maximum velocity of any velocity vector has to be lower than the bulk inlet velocity in the nozzle ($\overline{u}_{\text{inlet}}$). For the S-PIV dataset 99.5% of all instantaneous vector fields comply with this limit. Secondly, a local median test is performed on each vector relative to its neighboring vectors, specifically a normalized median test, as specified by Westerweel and Scarano (2005). Due to the limited size of the UIV probe, the values at the edges are symmetrically padded to enable a median check at the border of each measurement. Finally, a standard deviation check is performed, and each vector can deviate a maximum of 3 standard deviations

Fig. 8 Radial position of the recirculation location throughout the domain for different processing methods of UIV and the reference S-PIV measurements

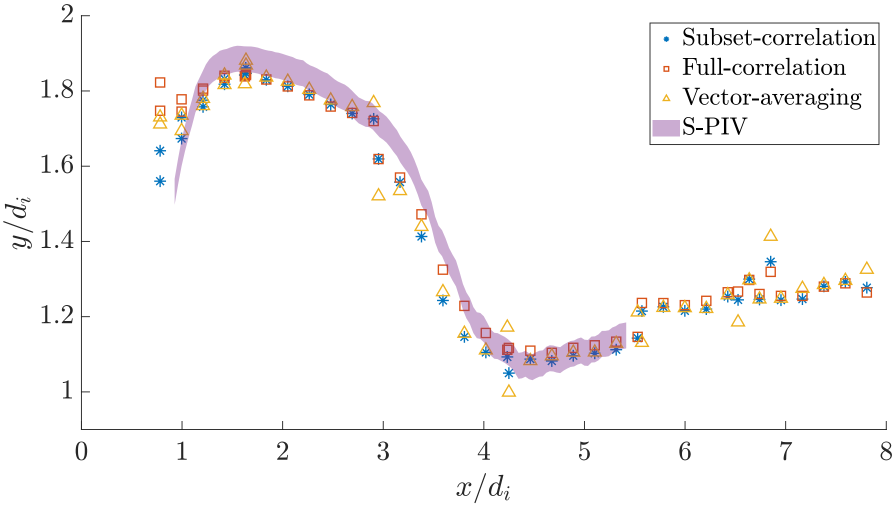

Fig. 9 Normalized correlation maps for the velocity vector at location $[x/d_\text{i};y/d_\text{i}] = [1.84;1.92]$, indicated with a round black circle in Fig. 7. The maps are plotted for the reference S-PIV measurement and for each correlation method of the UIV measurements

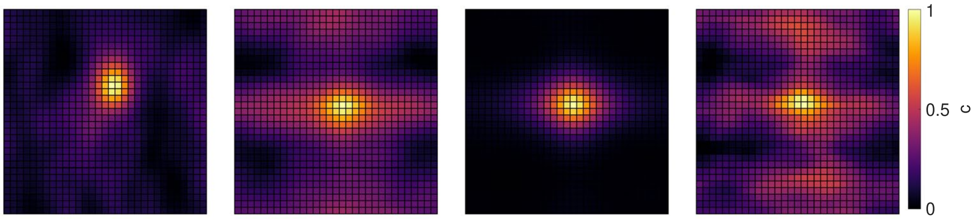

(a) S-PIV

(b) UIV, subset-correlation

(c) UIV, full-correlation

(d) UIV, vector-correlation

from the global mean for each velocity component. Conventionally, this value is between 3 and 5 for PIV (Raffel et al. 2018), the lower end is taken for this study since UIV data have higher standard deviations, especially deeper into the measurement volume. Any removed vector is linearly interpolated at the end of these post-processing steps. The fraction of removed vectors for each processing algorithm is lowest for full-correlation and highest for vector-averaging. At high values of *k*, the number of erroneous vectors can skew the median and standard deviation filters to have fewer vector rejections. Large pixel displacements are impossible to acquire because the flow is three-dimensional, and the particles leave the measurement plane between subsequent frames. This increases the importance of the subpixel fit, achieved through a 2D-gaussian fit, based on Nobach and Honkanen (2005). It is not straightforward to determine the uncertainty of the velocity vectors for the complex swirling flow at hand. Simply determining the standard deviation of the vector fields will not work, as this value comprises measurement noise and overall flow field variations. In order to discriminate both components, an uncertainty analysis is performed on a typical case at 50 vol%. In this approach one line of velocity vectors is selected, and a curve fit is applied to these data, depicted in Fig. 6.

It is assumed that the fit represents the average velocity field in the reactor. The deviation of the UIV data with respect to the fit is the measurement error. The standard deviation of the residuals (UIV measurements with respect to the fit) is found to be 4.6%. This is considered to be a typical value for the measurement noise in our study. Note that adjusting the UIV processing settings, such as the number of image pairs or interrogation window size, will influence this uncertainty (Geschwindner et al. 2022).

The speed of sound in the solid–liquid mixture is dependent on the volumetric concentration and particle size of the solids, by the formulas of Ament (1953), and the latter are an adaptation of Urick (1948). The intrinsic properties of water, glass, and PMMA are extracted from Lubbers and Graaff (1998), Kondo et al. (1981), and Amirkhani et al. (2011), respectively. All datasets are non-dimensionalized with $\overline{u}_{\mathrm{inlet}}$.

Table 1 Overview of the different UIV measurement campaigns, with the dominant temporal behavior included

Volumetric loading [vol%]	Pump frequency (f_{p}) [%]	$\dot{Q}$ [Lmin^{-1}]	Frequency (*f*) [Hz]	SNR [dB]	Strouhal number (St) [–10^{-3}]	Reynolds number [–]	Suspension Reynolds number [–]
0	45.6	18.5	[0.82–0.91]	9.0	[23–27]	17,900	Single-phase
20	62.5	25.9	[1.96–2.14]	5.6	[40–45]	26,200	14,100
20	100	42.7	[1.88–1.95]	3.3	[23–25]	44,400	23,900
30	100	40.5	[1.39–1.49]	2.6	[18–20]	43,900	15,100
40	87.5	28.1	[1.90–1.99]	5.0	[35–39]	29,200	5400
50	85.0	21.5	[1.72–1.80]	6.2	[42–46]	23,300	1600

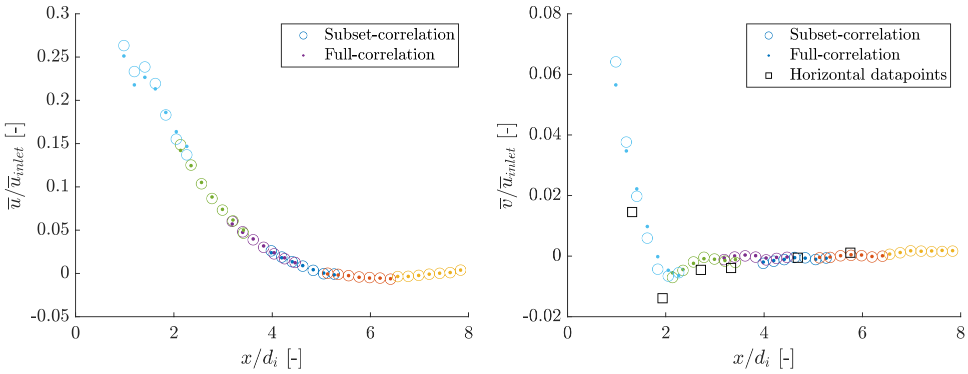

Fig. 10 Axial and radial velocity scattered for a line of vectors at $y/d_{\mathrm{i}} = 0.37$, for different datasets and both subset- and full-correlation-averaging at 50 vol%, $f_{\mathrm{p}} = 85\%$, and $\dot{Q} = 23.1\ L/min$

(a) Axial velocity of vectors at $^{y}/_{d_i} = 0.37$, with each dataset depicted in a different color.

(b) Radial velocity of vectors scattered at $^{y}/_{d_i} = 0.37$, with each dataset depicted in a different color, and also included the radial velocities of the horizontal subset-correlation-averaging datasets.

3 Single-phase flow measurements

First, single-phase measurements are performed using UIV to validate and compare the technique to a reference S-PIV case. Since the UIV transducer is only 38 mm wide, the measurements consist of multiple stitched datasets to reconstruct the flow field. A multi-pulse dataset is acquired for the UIV measurements. These UIV datasets are processed as subset-correlation, full-correlation, or vector-averaging and are compared to the S-PIV dataset. Figure 7 depicts the mean flow fields in a central cross section for both S-PIV and UIV datasets. A similar flow field, a Coandă jet flow (CoJF) with a central recirculation zone (CRZ), is noted for both the S-PIV and UIV measurements. This CRZ originates from a vortex breakdown in the nozzle and propagates through the domain due to the annular outlet. The vector-averaged dataset shows more inconsistencies, especially deeper into the measurement volume. The velocity close to the wall is lower for all UIV datasets compared to the S-PIV dataset. Deeper into the domain, the UIV datasets all overpredict the central recirculation velocity. The difference between S-PIV and each UIV dataset is similar for the three techniques since the error is inversely proportional to the square root of datapoints.

The recirculation location, where the flow reverses direction, is depicted in Fig. 8 throughout the reactor volume, for each dataset. If multiple crossings through zero are detected, the first encountered value is used. The error is equal to the spatial resolution of the vectors. Both the subset-correlation and full-correlation datasets have a high similarity with the S-PIV dataset. The vector-averaged dataset has a lower similarity to the S-PIV dataset. For some positions multiple datapoints are plotted due to the overlapping datasets.

Wall reflections are higher close to the wall and result in streaks of high correlation intensity. These reflections are also visible in the normalized correlation maps depicted in Fig. 9. The PIV results close to the wall are also prone to errors due to the curvature of the vessel. The S-PIV measurements have a clear correlation peak, while the subset-correlation results show a less distinct peak. The vector-averaged dataset shows more noise in the correlation plane, but averaging sufficient vector fields still gives reasonable results, as seen in Fig. 7d. Full-correlation-averaging isolates the peak more clearly. A peak can be identified for all correlation plots, for this specific vector.

The full-correlation datasets lacks temporal information, while the vector correlation dataset has higher instantaneous errors compared to the subset-correlation dataset. It is important to note that S-PIV separates the tangential velocity from the in-plane velocity data, while 2D measurement techniques include this tangential velocity as a perspective error to the in-plane data (Yoon and Lee 2002). In favor of UIV is that the image plane is the whole transducer itself, thereby minimizing this perspective error since no image projection is present. A time-domain spectral analysis for each vector, using Welch's power spectral density (PSD) (Welch 1967), is done on the S-PIV dataset and the UIV subset-correlation dataset, resulting in a dominant frequency of 0.86 ± 0.04 and 0.87 ± 0.05 Hz, respectively. Based on the above results and discussion, subset-correlation-averaging is applied for further analysis in this study.

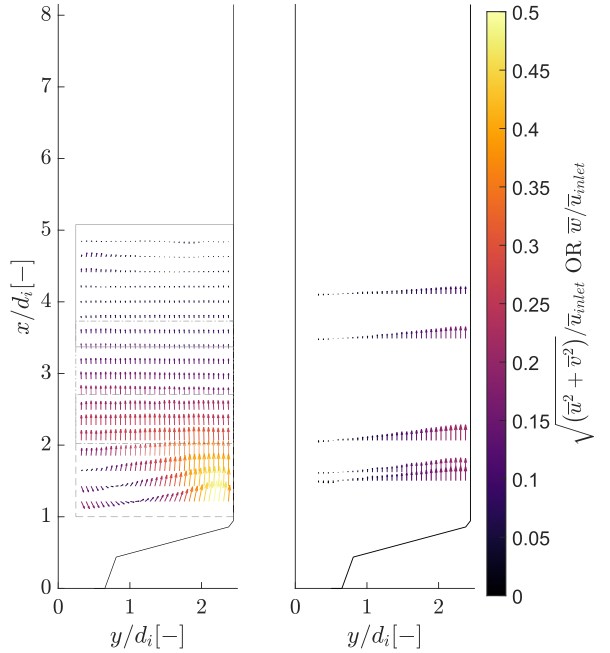

(a) Velocity magnitude of radial and axial velocity in a vertical plane. Each UIV measurement domain is shown with a grey box with a distinctive line pattern.

(b) Tangential velocity in multiple horizontal lines, depicting the legend for both subplots at the side.

Fig. 11 Velocity magnitude in a vertical plane and tangential velocity at multiple horizontal positions in an SFR at 20 vol% and $f_p = 62.5\%$, with $\dot{Q} = 25.9\ \mathrm{L\ min^{-1}}$

4 Dispersed phase flow measurements in a dense suspension

Solid particles are added to the system and four volumetric concentrations are measured, ranging from 20 to 50 vol%. An overview of all measurements, including some key characteristics, is shown in Table 1. The particles are weighed to determine the volumetric concentration in the 2 L reactor. The previously defined cost function, Eq. 3, is maximized for each specific vector. Measurements are only performed in areas where sufficient particles are present since UIV uses particles as tracers. Horizontal measurements are included for the suspension flow measurements, resulting in one line of vectors since reactor wall's curvature renders the other vectors unreliable, as indicated by the hatched area in Fig. 1a. At low flow rates and for all volumetric concentrations, it is observed that particles remain settled due to their higher density ($\rho_p/\rho_w = 2.57$).

In the vertical plane datasets, overlap is included to check for inconsistencies. All the datasets showed consistent velocity fields without sudden jumps between datasets. Figure 10 shows a representative figure for both axial and radial velocities at 50 vol% and $f_p = 85\%$. For the radial velocities, the data from the horizontal datasets are incorporated, demonstrating reasonable agreement with the radial velocities of the vertical datasets. The spread increases for measurements deeper into the domain, but the datasets remain consistent overall.

At 20 vol%, the just suspended condition ($f_p = 60\%$) is measured with UIV, as well as the maximum flow rate ($f_p = 100\%$). As the volumetric loading increases, the visually most homogeneous flowrate is measured. At 30 vol%, this occurs at maximum flow rate while for higher solid loading, this rate is reduced to prevent particle accumulation at the filter. Thus, homogeneity depends on the flow rate up to a certain volumetric loading. Beyond this point, particles accumulate at the top, necessitating a decrease in flow rate to enhance homogeneity. The temporal analysis provides a range of frequencies for each dataset. In the temporal domain, a wider peak compared to the single-phase measurements, is observed after performing a time-domain spectral analysis. A time-resolved dataset, with acquisition frequency of 7,500 Hz and a sliding sum-of-correlation of 10 frames, is used to check for higher frequencies ($\geq$ 3 Hz). The subset-correlation dataset's Nyquist frequency is around 3 Hz, while the time-resolved dataset's Nyquist frequency is 375 Hz. No dominant frequencies, between 3 and 375 Hz, are detected at either

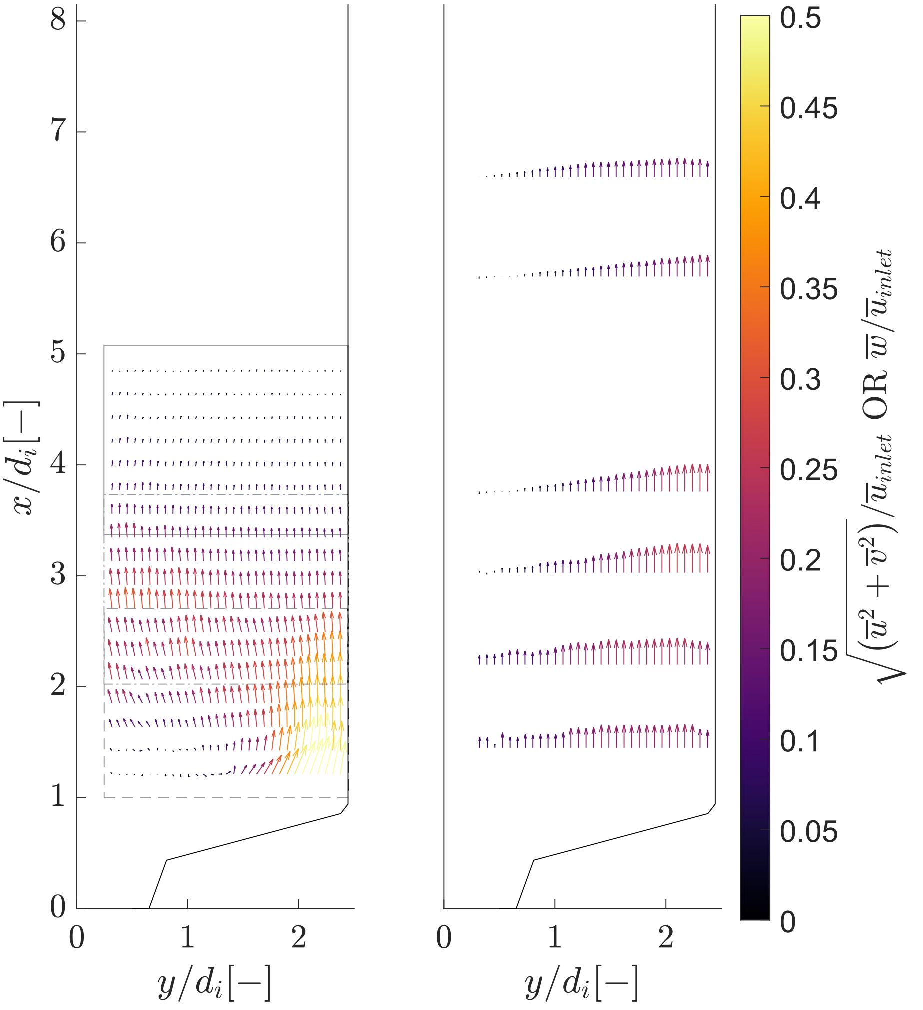

(a) Velocity magnitude of radial and axial velocity in a vertical plane. Each UIV measurement domain is shown with a grey box.

(b) Tangential velocity in multiple horizontal lines, depicting the legend for both subplots at the side.

Fig. 12 Velocity magnitude both in a vertical plane and at multiple horizontal positions in an SFR at 20 vol% and $f_p = 100\%$ with $\dot{Q} = 42.7\,\mathrm{L\,min^{-1}}$

Fig. 13 Velocity magnitude in a vertical plane and tangential velocity at multiple horizontal positions in an SFR at 30 vol% and $f_p = 100\%$, with $\dot{Q} = 40.5\,\mathrm{L\,min^{-1}}$

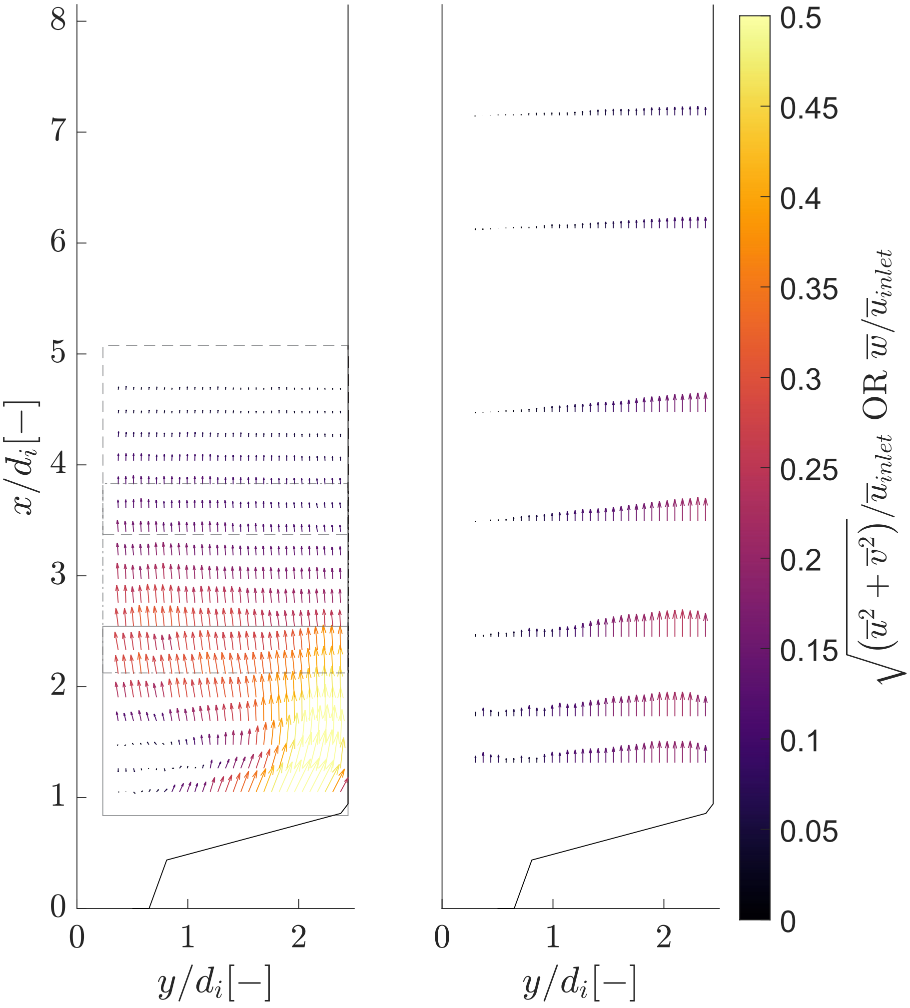

(a) Velocity magnitude of radial and axial velocity in a vertical plane. Each UIV measurement domain is shown with a grey box.

(b) Tangential velocity in multiple horizontal lines, depicting the legend for both subplots at the side.

20 vol% or 30 vol%. Consequently, these time-resolved measurements were not performed for higher volumetric concentrations and an optimization for the processing algorithm, for example pyramid-sum-of-correlation (Sciacchitano et al. 2012), was not considered. Each dataset is processed individually, and their temporal spectra are summed if there is at least one peak 3 dB higher than its average value, corresponding to a SNR of 3. The SNR of the summed spectra is noted in Table 1. The spread of the final peak value is assumed at the intersections of 50% of the peak height. The minimum and maximum value of all datasets is shown in Table 1. Introducing the glass particles increases the observed frequency compared to the single-phase flow for every measurement. Increasing the flow rate decreases the frequency only slightly, as observed for the 20 vol% case at both 27.2 and 44.6 L min^{-1}. No clear relations follow from the data shown in Table 1.

In a CFD simulation of the SFR, Yang et al. (2022) found a frequency of 0.373 Hz, corresponding to $St = 0.0106$ for a methanol–wood suspension with a Reynolds number of 130,000 and a Suspension Reynolds number of 70,000 at 20 vol%. Subsequent research (Yang et al. 2023) only shows a dominant frequency of 36 Hz and its second harmonic at 72 Hz, corresponding to St of 1 and 2. However, the total acquisition time of their dataset is too short to capture the low frequencies found in the current study. The Stokes number in Yang et al. (2023) is 0.31, compared to a maximum of 64 for the current study. This difference prohibits these high-frequency fluctuations from being present in the solid's phase velocity fields.

Visualization of the results of UIV measurements is shown in Figs. 11, 12, 13, 14 and 15, where either the in-plane velocities or the tangential velocity is plotted. The tangential maximum velocity is found downstream of the axial

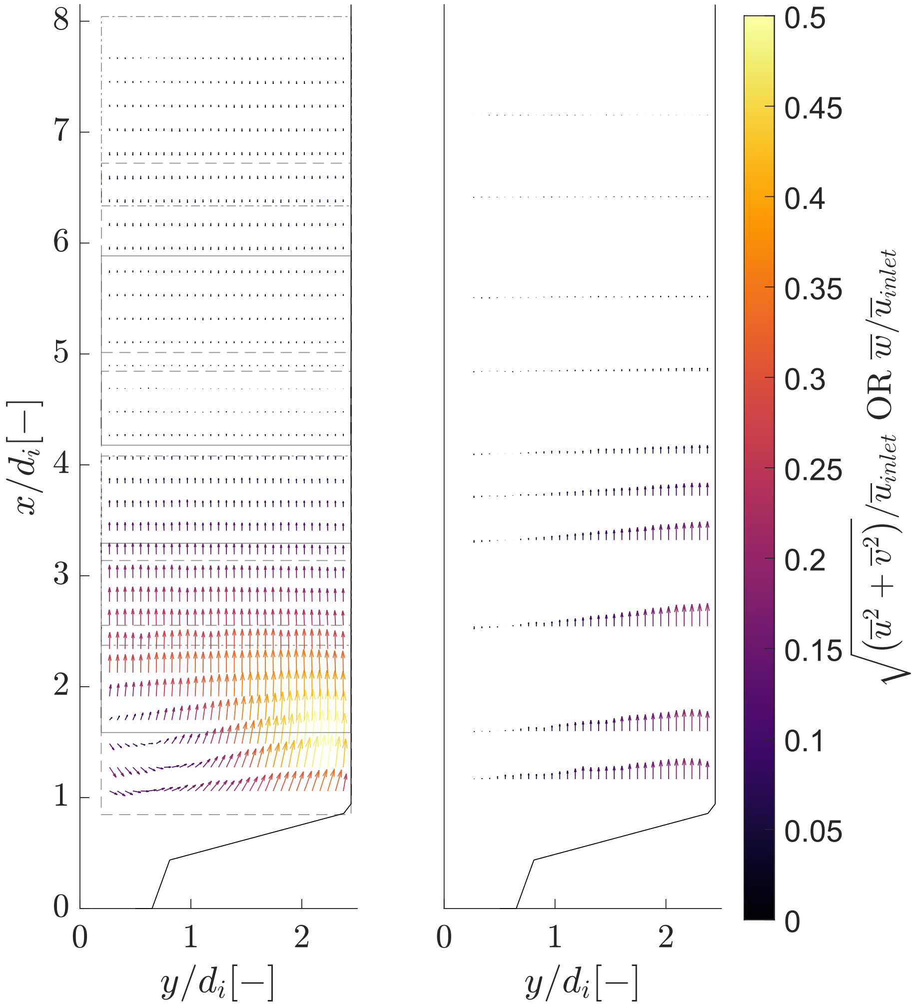

Fig. 14 Velocity magnitude in a vertical plane and tangential velocity at multiple horizontal positions in an SFR at 40 vol% and f_p = 85%, with $\dot{Q} = 28.1\,\mathrm{L\,min^{-1}}$

(a) Velocity magnitude of radial and axial velocity in a vertical plane. Each UIV measurement domain is shown with a grey box.

(b) Tangential velocity in multiple horizontal lines, depicting the legend for both subplots at the side.

maximum velocity for all measurements. A CoJF flow field is visible in each measurement, with a recirculation within the measurement region for the lower flow rate measurements. Compared to the single-phase flow measurements, the CRZ is pushed toward the center. For higher flow rates, the CRZ is no longer clearly visible on the UIV measurements due to its limited depth field (Figs. 12 and 13). Due to both refractions and reflections of the signal on the different medium interfaces, the SNR decreases with increasing depth of measurement. Some velocity fields seem to break continuity by having only positive axial velocities. However, mass flow is not necessarily linearly related to velocity, since only the dispersed phase is measured without indicating concentration, so these velocity fields can still be physical. The tangential velocities show some flow reversal before the center of the reactor, indicating a counter-rotating vortex core, as observed already for low-swirl flows by Vanierschot (2018).

The favorable mixing characteristics of an SFR are confirmed, based on these quantitative UIV measurements The envisioned CoJF is present at all studied flow conditions, avoiding sedimentation in the SFR. Increasing the volumetric loading increases the importance of finetuning the flow rate to avoid particle packing against the downstream filter.

5 Conclusions

In this work, the adaptability of UIV in accurately measuring the complex swirling flow within a swirling flow reactor (SFR) is demonstrated, extending its application beyond traditional 2D flow topologies. A good correspondence is found between UIV and S-PIV for the velocity fields and the temporal dynamics of a single-phase flow. Multiple bulk velocities and volume concentrations, even

Fig. 15 Velocity magnitude in a vertical plane and tangential velocity at multiple horizontal positions in an SFR at 50 vol% and $f_p = 85\%$, with $\dot{Q} = 22.0\,\mathrm{L\,min^{-1}}$

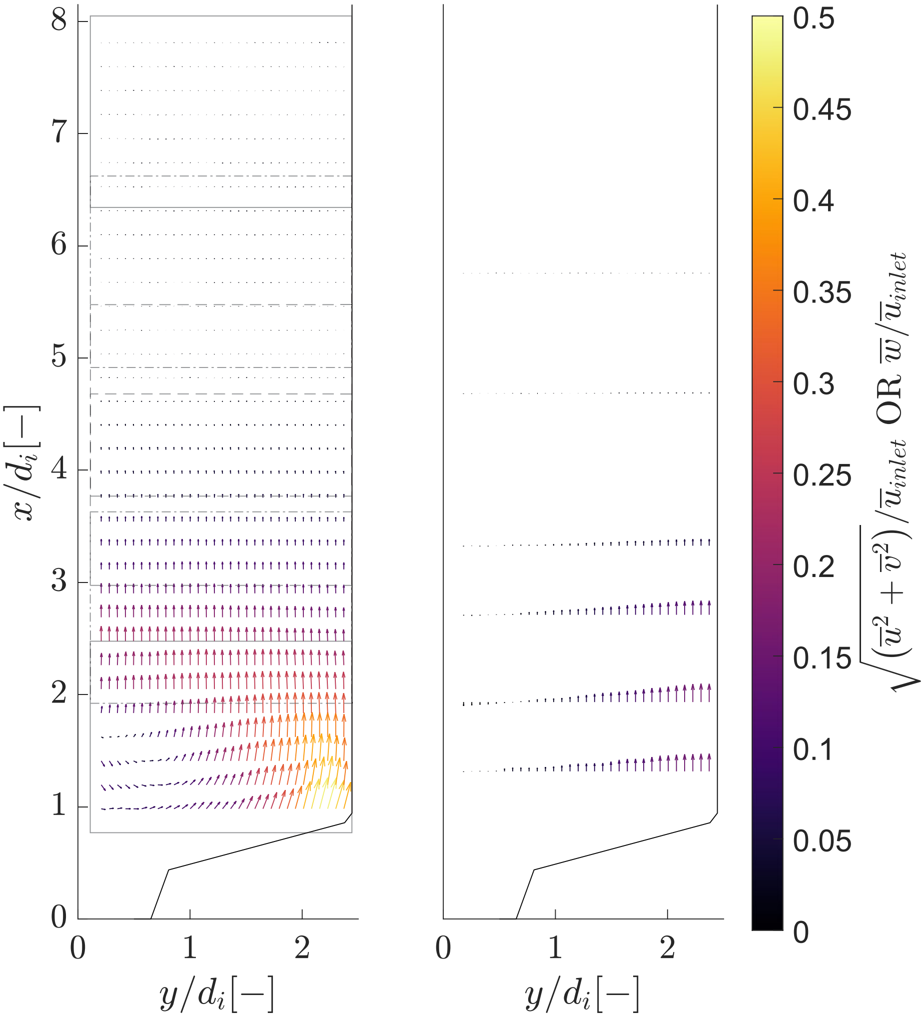

(a) Velocity magnitude of radial and axial velocity in a vertical plane. Each UIV measurement domain is shown with a grey box.

(b) Tangential velocity in multiple horizontal lines, depicting the legend for both subplots at the side.

up to 50 vol%, are examined with UIV using 2.3 mm glass beads in two transducer orientations, capturing indications of all three velocity components. Additionally, implementing an automated timestep optimization process proved crucial in managing high acquisition frequencies, enhancing data processing efficiency, and maintaining temporal dynamics. A low frequency (around 1–2 Hz) is identified in each flow field, with no clear relation to volumetric loading or flow rate. The operational principle of an SFR is successfully validated, achieving a uniform suspension through the observed CoJF pattern up until 50 vol% of solids loading. The findings also suggest potential insights into flow dynamics, such as the possible presence of a counter-rotating vortex core indicated by tangential velocity fields. Additionally, the CRZ present in single-phase flow is pushed toward the reactor's center, especially for higher flow rates. The conclusions can be summarized in the following points:

- CoJF is identifiable for all considered measurements, which confirms the working principle of an SFR.
- Even at high volumetric concentration (up to 50 vol%), quantitative measurements with UIV are possible.
- Correlation averaging within one subset is suited for data-processing to achieve a high SNR, while maintaining temporal information. A local timestep optimization increases the quality of the data.
- The researchers suggest to study different sizes, specific densities and flow rates to obtain more insights into the flow phenomena, preferably obtaining a regime map of parameters where an SFR achieves mixing.

Author Contributions [TH, WH, MV] contributed to conceptualization, formal analysis and investigation; [TH, WH] contributed to

methodology; [TH] performed experiments and writing—original draft preparation; [TH, WH, JDG, CP, MV] performed writing—review and editing; [TH, MV] contributed to funding acquisition; [WH, CP, MV] provided resources; [WH, JDG, MV] performed supervision.

Funding The funding of this research by the 'Dienst OnderzoeksCoördinatie (DOC) KU Leuven' through grant number C3/19/015 is gratefully acknowledged. Fonds voor Wetenschappelijk Onderzoek (FWO) is gratefully acknowledged for funding the research stay at TU Delft through Grant Number K221623N.

Availability of data and materials All data used in this study are available, on request, with the corresponding author.

Declarations

Conflict of interest The authors have no conflict of interest to declare that are relevant to the content of this article.

Ethical approval Not applicable.

References

Ament WS (1953) Sound propagation in gross mixtures. J Acoust Soc Am 25(4):638–641. https://doi.org/10.1121/1.1907156.

Amirkhani M, Taschin A, Cucini R, Bartolini P, Leporini D, Torre R (2011) Polymer thermal and acoustic properties using heterodyne detected transient grating technique. J Polym Sci Part B: Polym Phys 49(9):685–690. https://doi.org/10.1002/polb.22233.

Barabash VM, Abiev RS, Kulov NN (2018) Theory and practice of mixing: a review. Theor Found Chem Eng 52(4):473–487. https://doi.org/10.1134/S004057951804036X.

Barnes M, Zhang K, Rival D (2024) Lagrangian study of entrainment for confined vortex rings in dense suspensions using echo-LPT. Exp Fluids 65(3):33. https://doi.org/10.1007/s00348-024-03767-3.

Brändle De Motta JC, Costa P, Derksen JJ, Peng C, Wang L-P, Breugem W-P, Estivalezes JL, Vincent S, Climent E, Fede P, Barbaresco P, Renon N (2019) Assessment of numerical methods for fully resolved simulations of particle-laden turbulent flows. Comput Fluids 179, 1–14 (2019) https://doi.org/10.1016/j.compfluid.2018.10.016. Accessed 20 Sept 2024

Brum J, Bernal M, Barrere N, Negreira C, Cabeza C (2021) Vortex dynamics and transport phenomena in stenotic aortic models using Echo-PIV. Phys Med Biol 66(5):055026. https://doi.org/10.1088/1361-6560/abd670.

Carletti C, Montante G, Westerlund T, Paglianti A (2014) Analysis of solid concentration distribution in dense solid-liquid stirred tanks by electrical resistance tomography. Chem Eng Sci 119:53–64. https://doi.org/10.1016/j.ces.2014.07.049

Dash A, Hogendoorn W, Poelma C (2021) Ultrasonic particle volume fraction profiling: an evaluation of empirical approaches. Exp Fluids 62(4):85. https://doi.org/10.1007/s00348-020-03132-0.

Dash A, Hogendoorn W, Oldenziel G, Poelma C (2022) Ultrasound imaging velocimetry in particle-laden flows: counteracting attenuation with correlation averaging. Exp Fluids 63(3):56. https://doi.org/10.1007/s00348-022-03404-x.

Deen NG, Westerweel J, Delnoij E (2002) Two-phase PIV in bubbly flows: status and trends. Chem Eng Technol 25(1):97–101

Desmond KW, Weeks ER (2014) Influence of particle size distribution on random close packing of spheres. Phys Rev E 90(2):022204. https://doi.org/10.1103/PhysRevE.90.022204. Publisher: American Physical Society. Accessed 08 Apr 2024

Dijksman JA, Rietz F, Lőrincz KA, Van Hecke M, Losert W (2012) Invited article: refractive index matched scanning of dense granular materials. Rev Sci Instrum 83(1):011301. https://doi.org/10.1063/1.3674173.

Dugué J, Weber R (1992) Design and calibration of a 30kw natural gas burner for the University of Michigan. Technical Report, International Flame Research Foundation (IFRF), Ijmuiden, The Netherlands. Issue: C74/y/1

Eilers H (1941) Die Viskosität von Emulsionen hochviskoser Stoffe als Funktion der Konzentration. Kolloid-Zeitschrift 97(3):313–321. https://doi.org/10.1007/BF01503023.

Ferrini F, Ercolani D, De Cindio B, Nicodemo L, Nicolais L, Ranaudo S (1979) Shear viscosity of settling suspensions. Rheol Acta 18(2):289–296. https://doi.org/10.1007/BF01542776.

Fraser KH, Poelma C, Zhou B, Bazigou E, Tang M-X, Weinberg PD (2017) Ultrasound imaging velocimetry with interleaved images for improved pulsatile arterial flow measurements: a new correction method, experimental and in vivo validation. J R Soc Interface 14(127):20160761. https://doi.org/10.1098/rsif.2016.0761.

Geschwindner C, Westrup K, Dreizler A, Böhm B (2022) Ultra-high-speed time-resolved PIV of turbulent flows using a continuously pulsing fiber laser. Exp Fluids 63(4):75. https://doi.org/10.1007/s00348-022-03424-7

Gurung A, Poelma C (2016) Measurement of turbulence statistics in single-phase and two-phase flows using ultrasound imaging velocimetry. Exp Fluids 57(11):171. https://doi.org/10.1007/s00348-016-2266-x.

Hain R, Kähler CJ (2007) Fundamentals of multiframe particle image velocimetry (PIV). Exp Fluids 42(4):575–587. https://doi.org/10.1007/s00348-007-0266-6.

Hogendoorn W, Poelma C (2018) Particle-laden pipe flows at high volume fractions show transition without puffs. Phys Rev Lett 121(19):194501. https://doi.org/10.1103/PhysRevLett.121.194501.

Hogendoorn W, Chandra B, Poelma C (2021) Suspension dynamics in transitional pipe flow. Phys Rev Fluids 6(6):064301. https://doi.org/10.1103/PhysRevFluids.6.064301.

Hogendoorn W, Satish GC, Poelma C (2023) The spatial development of dense particle-laden pipe flows. San Diego State University, San Diego

Hogendoorn W, Poelma C (2019) High frame rate flow measurement using Ultrasound Imaging Velocimetry. In: Proceedings of the 13th International Symposium on Particle Image Velocimetry. Institute of Fluid Mechanics and Aerodynamics, Universität der Bundeswehr München, Germany, Munich, Germany. https://doi.org/10.18726/2019_3 . https://pure.tudelft.nl/ws/portalfiles/portal/62630916/129135.pdf Accessed 07 Feb 2024

Holemans T, Yang Z, De Greef J, Vanierschot M (2023) Experimental study of a self-excited jet precession in a sudden expansion flow. Exp Fluids 64(5):107. https://doi.org/10.1007/s00348-023-03650-7.

Holemans T, Yang Z, De Greef J, Vanierschot M (2024). Swirl-induced hysteresis in a sudden expansion flow https://doi.org/10.2139/ssrn.4798243. https://www.ssrn.com/abstract=4798243 Accessed 19 Apr 2024

Holemans T, Yang Z, De Greef J, Vanierschot M (2023) Simultaneous Existence of a Coandã and Central Jet Flow measured by Stereoscopic Particle Image Velocimetry. In: Proceedings of the 15th international symposium on particle image velocimetry, San Diego, USA

Hoving AM, Voorneveld J, Mikhal J, Bosch JG, Groot Jebbink E, Slump CH (2021) In vitro performance of echoPIV for assessment of laminar flow profiles in a carotid artery stent. J Med Imaging 8(01). https://doi.org/10.1117/1.JMI.8.1.017001 Accessed 25 Jan 2024

Jaszczur M, Młynarczykowska A (2020) A general review of the current development of mechanically agitated vessels. Processes 8(8):982. https://doi.org/10.3390/pr8080982.

Kondo K-I, Iio S, Sawaoka A (1981) Nonlinear pressure dependence of the elastic moduli of fused quartz up to 3 GPa. J Appl Phys 52(4):2826–2831. https://doi.org/10.1063/1.329012.

Kuzmin AO (2021) Confined multiphase swirled flows in chemical engineering. Rev Chem Eng 37(1):31–68. https://doi.org/10.1515/revce-2019-0019.

Li G, Gao Z, Li Z, Wang J, Derksen JJ (2018) Particle-resolved PIV experiments of solid-liquid mixing in a turbulent stirred tank. AIChE J 64(1):389–402. https://doi.org/10.1002/aic.15924.

Lubbers J, Graaff R (1998) A simple and accurate formula for the sound velocity in water. Ultrasound Med Biol 24(7):1065–1068. https://doi.org/10.1016/S0301-5629(98)00091-X.

Meinhart CD, Wereley ST, Santiago JG (2000) A PIV algorithm for estimating time-averaged velocity fields. J Fluids Eng 122(2):285–289. https://doi.org/10.1115/1.483256.

Montante G, Paglianti A, Magelli F (2012) Analysis of dilute solid–liquid suspensions in turbulent stirred tanks. Chem Eng Res Des 90(10):1448–1456. https://doi.org/10.1016/j.cherd.2012.01.009.

Nobach H, Honkanen M (2005) Two-dimensional Gaussian regression for sub-pixel displacement estimation in particle image velocimetry or particle position estimation in particle tracking velocimetry. Exp Fluids 38(4):511–515. https://doi.org/10.1007/s00348-005-0942-3.

Oberkampf WL, Trucano TG (2002) Verification and validation in computational fluid dynamics. Prog Aerosp Sci 38(3):209–272. https://doi.org/10.1016/S0376-0421(02)00005-2.

Pangarkar VG (2017) Process intensification in multiphase reactors: from concept to reality. Chem Eng Process Process Intensif 120:1–8. https://doi.org/10.1016/j.cep.2017.06.004

Poelma C (2017) Ultrasound imaging velocimetry: a review. Exp Fluids 58(1):3. https://doi.org/10.1007/s00348-016-2283-9.

Poelma C (2020) Measurement in opaque flows: a review of measurement techniques for dispersed multiphase flows. Acta Mech 231(6):2089–2111. https://doi.org/10.1007/s00707-020-02683-x.

Poelma C, Westerweel J, Ooms G (2006) Turbulence statistics from optical whole-field measurements in particle-laden turbulence. Exp Fluids 40(3):347–363. https://doi.org/10.1007/s00348-005-0072-y.

Poelma C, Mari JM, Foin N, Tang M-X, Krams R, Caro CG, Weinberg PD, Westerweel J (2011) 3D Flow reconstruction using ultrasound PIV. Exp Fluids 50(4):777–785. https://doi.org/10.1007/s00348-009-0781-8.

Raffel M, Willert CE, Scarano F, Kähler CJ, Wereley ST, Kompenhans J (2018) Particle image velocimetry: a practical guide. Springer, Cham. https://doi.org/10.1007/978-3-319-68852-7 . https://link.springer.com/10.1007/978-3-319-68852-7 Accessed 21 Dec 2023

Scarano F, Poelma C (2009) Three-dimensional vorticity patterns of cylinder wakes. Exp Fluids 47(1):69. https://doi.org/10.1007/s00348-009-0629-2.

Sciacchitano A, Scarano F, Wieneke B (2012) Multi-frame pyramid correlation for time-resolved PIV. Exp Fluids 53(4):1087–1105. https://doi.org/10.1007/s00348-012-1345-x

Shi P, Rzehak R (2020) Solid-liquid flow in stirred tanks: Euler–Euler/RANS modeling. Chem Eng Sci 227:115875. https://doi.org/10.1016/j.ces.2020.115875

Stickel JJ, Powell RL (2005) Fluid mechanics and rheology of dense suspensions. Annu Rev Fluid Mech 37(1):129–149. https://doi.org/10.1146/annurev.fluid.36.050802.122132.

Tanter M, Fink M (2014) Ultrafast imaging in biomedical ultrasound. IEEE Trans Ultrason Ferroelectr Freq Control 61(1):102–119. https://doi.org/10.1109/TUFFC.2014.2882.

Thielicke W, Stamhuis EJ (2014) PIVlab—towards user-friendly, affordable and accurate digital particle image velocimetry in MATLAB. J Open Res Softw 2 (2014) https://doi.org/10.5334/jors.bl. 19 Feb Accessed 2024

Urick RJ (1948) The absorption of sound in suspensions of irregular particles. J Acoust Soc Am 20(3):283–289. https://doi.org/10.1121/1.1906373.

Vanierschot M (2007) Fluid mechanics and control of annular jets with and without swirl. PhD thesis, KU Leuven, Leuven

Vanierschot M (2018) Large scale flow instabilities in sudden expansion flows in the subcritical swirl regime. In: Proceedings of 19th international symposium on application of laser and imaging techniques to fluid mechanics, Lisbon, Portugal, pp 2215–2224

Vanierschot M, Müller JS, Sieber M, Percin M, van Oudheusden BW, Oberleithner K (2020) Single- and double-helix vortex breakdown as two dominant global modes in turbulent swirling jet flow. J Fluid Mech 883:31. https://doi.org/10.1017/jfm.2019.872

Walker AM, Scott J, Rival DE, Johnston CR (2014) In vitro post-stenotic flow quantification and validation using echo particle image velocimetry (Echo PIV). Exp Fluids 55(10):1821. https://doi.org/10.1007/s00348-014-1821-6.

Welch P (1967) The use of fast Fourier transform for the estimation of power spectra: a method based on time averaging over short, modified periodograms. IEEE Trans Audio Electroacoust 15(2):70–73. https://doi.org/10.1109/TAU.1967.1161901

Westerweel J, Scarano F (2005) Universal outlier detection for PIV data. Exp Fluids 39(6):1096–1100. https://doi.org/10.1007/s00348-005-0016-6.

Wiederseiner S, Andreini N, Epely-Chauvin G, Ancey C (2011) Refractive-index and density matching in concentrated particle suspensions: a review. Exp Fluids 50(5):1183–1206. https://doi.org/10.1007/s00348-010-0996-8.

Wright SF, Zadrazil I, Markides CN (2017) A review of solid–fluid selection options for optical-based measurements in single-phase liquid, two-phase liquid–liquid and multiphase solid–liquid flows. Exp Fluids 58(9):108. https://doi.org/10.1007/s00348-017-2386-y.

Yang Z (2023) Design and optimization of a swirling flow reactor for solid–liquid mixing. PhD thesis, KU Leuven, Leuven

Yang Z, Holemans T, Lagrain B, Sels B, Vanierschot M (2022) Optimization of liquid–solid mixing by swirl using computational fluid dynamics simulations. KU Leuven, Leuven

Yang Z, Holemans T, Lagrain B, Sels B, Vanierschot M (2023) A solid–liquid mixing reactor based on swirling flow technology. Chem Eng Sci 280:119054. https://doi.org/10.1016/j.ces.2023.119054

Yoon J-H, Lee S-J (2002) Direct comparison of 2D PIV and stereoscopic PIV measurements. Meas Sci Technol 13(10):1631–1642. https://doi.org/10.1088/0957-0233/13/10/317

Zachos A, Kaiser M, Merzkirch W (1996) PIV measurements in multiphase flow with nominally high concentration of the solid phase. Exp Fluids 20(3):229–231. https://doi.org/10.1007/BF00190280.

Zhang Y, Vanierschot M (2021) Determination of single and double helical structures in a swirling jet by spectral proper orthogonal decomposition. Phys Fluids 33(1):015115. https://doi.org/10.1063/5.0032985.

Zhang F, Lanning C, Mazzaro L, Barker AJ, Gates PE, Strain WD, Fulford J, Gosling OE, Shore AC, Bellenger NG, Rech B, Chen J, Chen J, Shandas R (2011) In vitro and preliminary in vivo validation of echo particle image velocimetry in carotid vascular imaging. Ultrasound Med Biol 37(3):450–464. https://doi.org/10.1016/j.ultrasmedbio.2010.11.017